Photoacoustics 42 (2025) 100703

Contents lists available at ScienceDirect

Photoacoustics

journal homepage: www.elsevier.com/locate/pacs

All-fiber three-wavelength laser for functional photoacoustic microscopy

Mingxuan Yang [a], Zheng Qu [a], Mohammadreza Amjadian [a], Xu Tang [a], Jiangbo Chen [a,b,*], Lidai Wang [a,c,*]

[a] Department of Biomedical Engineering, City University of Hong Kong, 83 Tat Chee Ave, Kowloon, Hong Kong
[b] School of Mechanical and Automotive Engineering, South China University of Technology, 381 Wushan Road, Guangzhou 510640, China
[c] City University of Hong Kong Shenzhen Research Institute, Yuexing Yi Dao, Shenzhen, Guang Dong 518057, China

ARTICLE INFO

Keywords:
Photoacoustic microscopy
Stimulated Raman scattering
All-fiber system
Functional imaging

ABSTRACT

Advanced multi-wavelength pulsed laser is a key technique for functional optical-resolution photoacoustic microscopy (OR-PAM). By utilizing the stimulated Raman scattering (SRS) effect, we can generate various wavelengths from a single-wavelength pump laser, offering a simple and cost-effective solution for OR-PAM. However, existing multi-wavelength SRS lasers typically require fine alignment of many free-space optical components with single-mode fibers, which are susceptible to mechanical disturbances and temperature fluctuations, leading to high maintenance costs. To address this challenge, we develop an all-fiber three-wavelength SRS laser source for functional OR-PAM. A pump laser beam is launched into an optical fiber network, which splits and delays these laser pulses and generates different optical wavelengths in different fiber branches, and then merges them at the output end of the fiber network. This approach requires only one instance of fiber launching, dramatically simplifying the alignment and improving the laser stability. Using a decoding algorithm, we can separate the PA signals from different optical wavelengths and then calculate oxygen saturation (sO_2) and flow speed. The SRS fiber network provides stable energy ratios among different optical wavelengths during long-time operation. We use the all-fiber OR-PAM system to monitor the brain function for four hours, demonstrating exceptional stability in functional imaging. The small size, simple structure, and low cost make it suitable for many preclinical and clinical applications.

1. Introduction

Optical resolution photoacoustic microscopy (OR-PAM) has attracted significant attention due to its high-resolution, label-free functional imaging ability [1–15]. Advanced functional OR-PAM needs a multi-wavelength laser with high power, stable energy ratio, and rapid wavelength switching time [16–26]. Many commercial pulsed lasers with high power and high pulse repetition rates only offer a single optical wavelength. Other wavelengths must be generated using wavelength conversion techniques, such as dye laser [27] or optical parametric oscillation (OPO) [28–32]. Building a multi-wavelength laser system with multiple dye or OPO lasers is expensive and requires significant maintenance effort.

Stimulated-Raman-scattering(SRS)-based wavelength conversion is a simple and low-cost approach to generating new wavelengths and has been developed for OR-PAM [16,17,32–34]. With a pump laser, high-order Raman wavelengths can be produced using a long fiber. This fiber also introduces pulse delay, allowing photoacoustic signals from different wavelengths to be temporally separated by using a long fiber [26]. Consequently, optical wavelengths can be switched at high speed.

Despite these advantages, SRS-based multi-wavelength lasers face several challenges. First, many free-space optical components must be finely tuned to direct light into different fibers [35], making the laser system bulky and expensive. Second, launching into multiple single-mode fibers requires precise alignment and frequent maintenance. Achieving high coupling efficiency often necessitates adjusting the fiber couplers before each use, a time-consuming process. Relocating the free-space SRS laser system requires realigning all optics, hindering the development of portable or point-of-care imaging systems. Third, the efficiency of the SRS-based wavelength conversion is sensitive to pump laser power. Minor misalignment, vibrations of optical parts, air flow, or temperature changes can lead to significant pulse energy fluctuations across different wavelengths, increasing errors in spectral unmixing. Although laser energy fluctuations can be mitigated using a high-speed

---

* Corresponding authors at: Department of Biomedical Engineering, City University of Hong Kong, 83 Tat Chee Ave, Kowloon, Hong Kong.
E-mail addresses: cjiangbo@scut.edu.cn (J. Chen), lidawang@cityu.edu.hk (L. Wang).

https://doi.org/10.1016/j.pacs.2025.100703
Received 1 January 2025; Received in revised form 4 February 2025; Accepted 19 February 2025

photodiode, this adds complexity and cost. Therefore, reducing the number of fiber launches can significantly decrease system size and maintenance costs, improve stability, and expand the applications of OR-PAM.

We present an all-fiber SRS fiber laser technique for functional OR-PAM. This method uses multiple SRS-based wavelength conversions within an optical fiber network, requiring only one optical fiber launch at the input of the fiber network. Within the network, the pump laser beam is split and wavelength-shifted across different branches. Various optical wavelengths are delayed using fibers of different lengths, encoded with fixed pulse energy ratios, and then recombined at the output. This approach simplifies optical alignment and results in a more compact laser system. Additionally, because the energy ratios among different wavelengths are not affected by free-space optics, the long-term stability of the laser pulse energy is significantly enhanced. After data acquisition, photoacoustic signals from different wavelengths are unmixed based on their temporal delays and designated pulse energy ratios. In in vivo experiments, we demonstrate that the all-fiber OR-PAM (FPAM) achieves high-resolution functional imaging with exceptional stability. Moreover, we continuously monitored cortical hemodynamics and functions in response to caffeine intake for up to four hours. The FPAM effectively reveals local vasoconstriction, flow fluctuations, and deoxygenation within the cerebral cortex at the single-vessel level.

2. Methods

2.1. *All-fiber stimulated Raman scattering laser source and imaging system*

Fig. 1(a) shows the schematic of the all-fiber three-wavelength pulsed laser source and the OR-PAM probe. Compared with traditional SRS laser [25,26], the all-fiber SRS laser has fewer optical elements and a simpler structure. A 532-nm nanosecond pulsed laser (VGEN-G-30, Spectra-Physics) serves as the pump laser. The pump laser beam is launched into the network of single-mode fibers as shown in Fig. 1(b). In the fiber network, two 1 × 3 single-mode fiber couplers (FC_{in} and FC_{out}, each 1 × 3 coupler is implemented by cascading two 2 × 2 couplers (Jiu-optic technology Co., LTD), fiber model: 460-HP, Nufern) with different power ratios are used to split and merge the light beams. FC_{in} is a 1 × 3 coupler with a output power ratio of 46 %: 22 %: 32 %. Due to the limitations of laboratory conditions and to avoid the tedious work of adjusting the polarization of laser, we chose pure silica core single-mode fiber instead of polarization-maintaining pure silica core single-mode fiber. In Path 1, the 532-nm light passes directly to the output fiber coupler FC_{out}. Path 2 uses a 28-meter non-polarization maintained single-mode (NPMS) fiber (s-460-HP, Nufern) for producing 545-nm light via the SRS effect. Mixed with the pump light, the output wavelengths from the Path 2 include 532 and 545 nm. Path 3 uses a 40-meter NPMS fiber (s-460-HP, Nufern) for generating 545 and 558 nm light via the SRS effect. The output of Path 3 includes mixed 532, 545, and 558 nm light. The three paths are combined by a 3 × 1 coupler with a power ratio of 1:1:1. The fibers in the three paths offers different time delays among the three pulses, and thus the combined light forms a pulse train with three mixed wavelengths at designated power ratios. With the fiber lengths from ends of the coupler, the optical path differences between Path 1 and the other two paths are 31 m and 46 m respectively.

The photoacoustic imaging probe is the same as the one in [22]. An achromatic lens (AC064–013-A, Thorlabs Inc.) is used to collimate the laser beam from the fiber. The collimated beam is reflected by a mirror and then focused by an objective lens (AC064-013-A, Thorlabs Inc.). An optical/acoustic beam combiner reflects the focused laser beam onto the sample. An acoustic lens (AL #45-697, Edmund Optics Inc.) is adhered to the optical/acoustic beam combiner to collect the acoustic waves from the sample. The optical/acoustic beam combiner transmits the acoustic wave. An ultrasound transducer (50-MHz center frequency, 78 % bandwidth, V214-BC-RM, Olympus Inc.) is used to detect the acoustic wave. The signal from the transducer is amplified by two 24-dB amplifiers (ZFL-500LN+, Mini-Circuits). Two linear stages (PLS-85, Physik Instrument GmbH & Co. KG) translate the PA probe for raster scanning along the *x*- and *y*-axes. PA signal is digitized by an acquisition card at 500 MHz (ATS9360, Alazar Technologies Inc.). The lateral resolution of OR-PAM used is 3.24 μm while the axial resolution is 36 μm. The maximum imaging depth of the PAM is 0.78 mm [22].

2.2. *Spectral unmixing*

The pulse train from the fiber network consists of mixed optical wavelengths with fixed pulse energy ratios. As the Fig. 1(c) shows, by unmixing the PA signals, we can extract the PA signals X at each wavelength. We represent the pulse energies at the output port of the

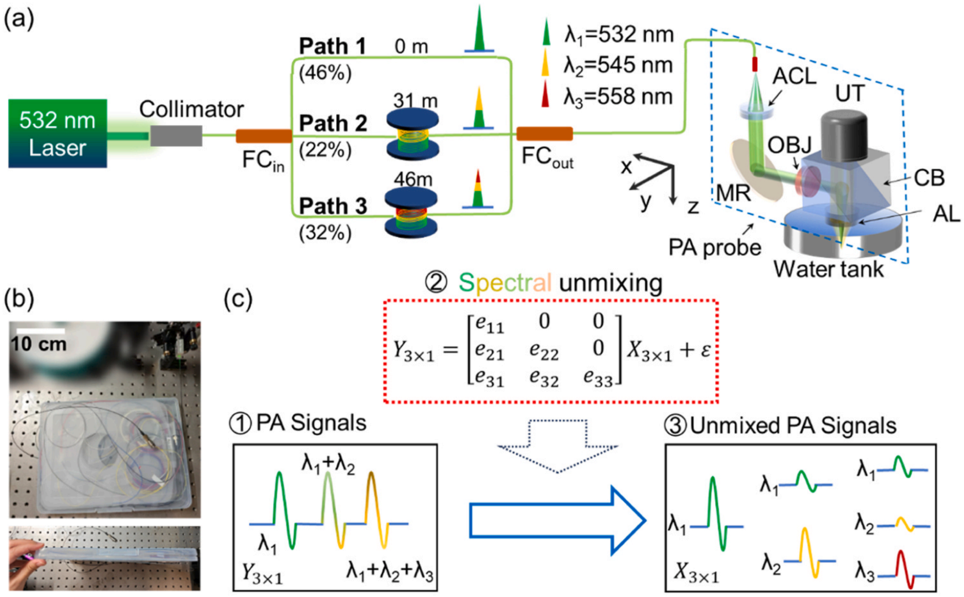

Fig. 1. (a) Schematic of all-fiber three-wavelength laser and OR-PAM probe. ACL, achromatic lens; AL, acoustic lens; CB, combiner; FC, fiber coupler; MR, mirror; OBJ, objective; UT, ultrasonic transducer. (b) Photograph of the all-fiber SRS system. (c) Schematic of PA signal decoupling in FPAM.

fiber network as an energy matrix A:

$$A = \left[e_{ij}\right] = \begin{bmatrix} e_{11} & 0 & 0 \\ e_{21} & e_{22} & 0 \\ e_{31} & e_{32} & e_{33} \end{bmatrix}, \tag{1}$$

where i represents the index of laser pulses, and j represents the index of optical wavelengths as 532, 545 and 558 nm. Fig. 2(a)–(c) shows the pulse train energy at different wavelengths after optical filters detected by high speed photodiode (DET025A, Thorlabs Inc.). Fig. 2(a) shows the 532-nm light components ($e_{11}, e_{21,} e_{31}$) from three pulses while Fig. 2(c) only shows the 558-nm light from the last pulse(e_{33}). By integrating the photodiode signals, the energy matrix A can be pre-calibrated before each experiments. The optical pulse train induce three temporally separated PA signals that can be expressed as

$$Y = AX + \varepsilon, \tag{2}$$

where Y is a 3 × 1 vector representing peak-to-peak values of three A-line signals excited by the pulse train, A is the pre-calibrated energy matrix, X is the unmixed PA signals amplitudes with unit excitation energy at each wavelength λ_j, and ε are random noises.

We use the SRS effect in the optical fiber to produce the 545 and 558-nm wavelengths. To achieve high power, it is necessary to keep the optical fiber short. Here, we use 31-m and 46-m fibers in Path 2 and 3, which results in a 75-ns delay between them. Consequently, the PA signals from pulses 2 and 3 may exhibit little overlap. We first use a two-step proximal gradient descent algorithm to separate the overlapped PA signals, then use the separated PA signals from the three pulses to solve Eq. (2). The detailed method for separating overlapped signals can be found in our previous publication [36].

3. Results

3.1. Stability and cost analysis

Stability of the SRS pulse energy is of great importance in the calculation of oxygen saturation and is primarily affected by the space-to-fiber coupling. We assume that the stable probability is p $(0 < p < 1)$ for one space-to-fiber coupler. In a traditional SRS laser system with n wavelengths, there are at least $2n$-1 fiber couplers, resulting in a stable probability of $p^{(2n-1)}$. In contrast, the all-fiber SRS laser system contains only one coupler with a stable probability of p. Therefore, the all-fiber SRS laser system is expected to be more stable than the free-space approach, and this advantage will become more pronounced as the number of wavelengths increases.

To validate the long-term stability, we measured the pulse energy from the all-fiber optical paths used in FPAM and compared it with the three individual fibers approach in traditional PAM (TPAM). The traditional PAM use the 25-m NPMS fiber (s-460-HP, Nufern) for producing 545-nm light. While another 47-meter NPMS fiber (s-460-HP, Nufern) is used for producing 558-nm light.We use the 532-nm pump pulse energy as the reference and define an energy ratio R as follows to represent the relative pulse energy fluctuation:

$$R = \sqrt{\left(\frac{e_{p2}}{e_{p1}}\right)^2 + \left(\frac{e_{p3}}{e_{p1}}\right)^2} \tag{3}$$

where e_{pi} is the ith pulse energy measured by a high-speed photodetector. We measured the energy ratio R by 1000 times per hour for 10 h. To avoid the fluctuation of pump laser, Fig. 2.(d) and (e) are recorded alternately with the same pump laser. The gray shadow indicating the standard deviations in every hour. In a 10-hour test, the pulse energy ratio of the all-fiber SRS laser changes less than ~ 2 %; while the pulse energy ratio of the traditional SRS laser varies up to 46 %, 23 times greater than that of the all-fiber approach. Moreover, once the light is launched into the fiber network, the energy ratio among different paths will remain constant, which increases the pulse-to-pulse stability of the energy ratio. The pulse-to-pulse fluctuation (standard deviation) of the all-fiber SRS laser is 0.0035, which is much less than that of the traditional SRS laser (0.0401). We also tested the fluctuation of energy matrix A in 8 seperated experiments (normalized by e_{11}). The averaged energy and its standard deviation in Fig. 2(f) further demonstrate the ease of use of the all-fiber SRS laser. These results indicate that the use of only one fiber coupler increases the pulse energy stability in both pulse-to-pulse and long-term operations.

In addition to its superior stability, the all-fiber SRS laser significantly reduces the size and maintenance cost. As shown in Fig. 1. (b), all of the SRS fibers can be housed in an A4-sized box. We only need to focus one free-space beam into a single-mode fiber, making adjustments and maintenance easy. Moreover, we use an unmixing algorithm, instead of

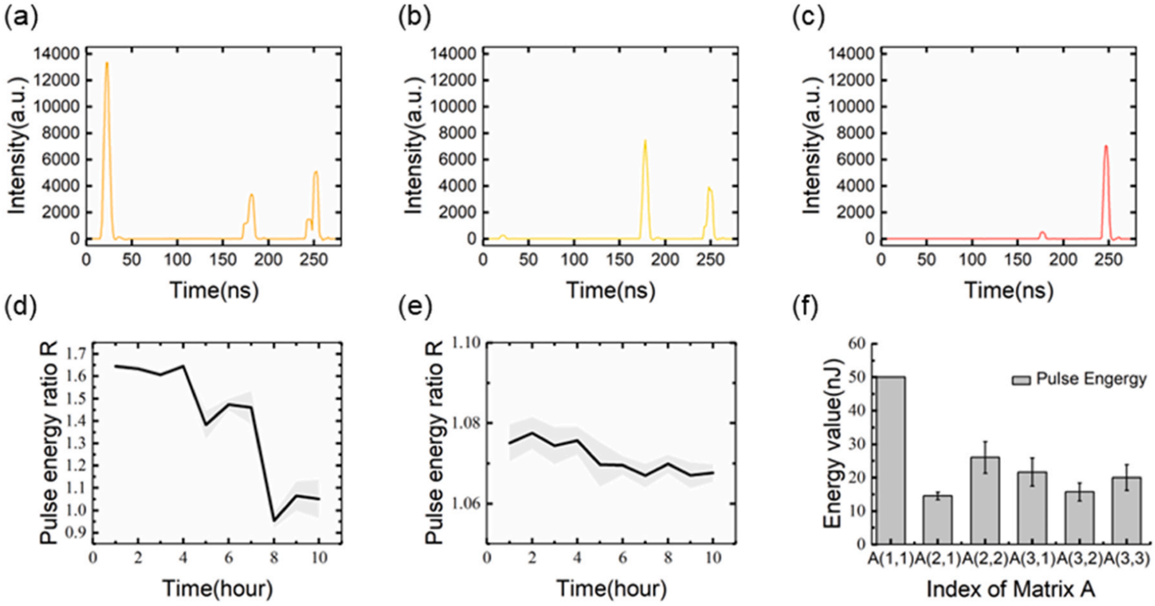

Fig. 2. All-fiber SRS laser pulses recorded by a photodiode after (a) a 532-nm bandpass filter, (b) a 545-nm bandpass filter, and (c) a 558-nm bandpass filter. Long-term pulse energy stability of (d) traditional SRS laser and (e) all-fiber OR-PAM. The pulse energy ratio R is calculated from the pulse energies across three pulses.(f) shows the fluctuation of pulse energy matrix in 8 different experiments.

multiple bandpass filters, to separate different wavelengths, lowering hardware costs and improving energy efficiency. When the number of paths increases beyond two, both complexity and cost increase considerably; in comparison, the all-fiber approach is more scalable. However, commercial couplers restricts the maximum average power to 10 mW which restricts the application of the all-fiber SRS system in high speed OR-PAM. With customized pure silica core couplers, we may further improve our all-fiber SRS laser for fast scanning OR-PAM [25] in the near future.

3.2. *In vivo functional imaging*

We tested the accuracy and stability of in vivo functional imaging. ICR mice at 5-weeks old were used for imaging. The pulse repetition rate of the pump laser is 4 kHz, and the pump pulse width is 7 ns. The pulse energy at each wavelength is below 60 nJ for all in vivo experiments. When the light is focused at 200 μm below the tissue surface, the optical fluence is 6.9 mJ/cm^2, within the American National Standards Institute (ANSI) safety limit (20 mJ/cm^2). Healthy mice were imaged under normal physiological conditions in the following experiments. The animal experiments were approved by the Animal Ethics Committee of the City University of Hong Kong.

In the experiments, we acquired two sets of multi-wavelength images of the same region of interest using the all-fiber and traditional PAM systems. For the all-fiber PAM data, we unmixed the 532 and 558-nm images to calculate sO$_2$. First, we measured the average pulse energies of each wavelengths in the pulse train. To be specific, we directed the output laser through different bandpass filters and illuminated it onto a high-speed photodetector as Fig. 2. (a)–(c) show. This allowed us to determine the energy of a specific wavelength in different pulses, as shown below:

$$A = \begin{bmatrix} 50 & 0 & 0 \\ 14.5 & 26 & 0 \\ 21.6 & 15.7 & 20 \end{bmatrix}. \tag{4}$$

The unit is nanojoule (nJ). By solving Eq. (2) at each A-line, we can separate the PA signals at 532, 545, and 558 nm. Similarly, by using the unmixed PA signals at 532 nm and 558 nm, we can calculate the sO$_2$ map. For comparison, we computed the sO$_2$ images using the traditional PAM data at 532 and 558 nm. The SRS systems are the same as the one used in previous section.

Fig. 3(a) and (c) show that both traditional and all-fiber PAM can reveal the oxygenation of the microvessels when the systems were well-tuned at time 0. The slope of the fitted line in Fig. 3(e) is 0.96, suggesting that the sO$_2$ values resolved by FPAM are nearly identical to those obtained by TPAM. After 3 h, the slope changed to 0.98 in Fig. 3(f), indicating the high similarity between Fig. 3(c) and Fig. 3(d). However, as illustrated in Fig. 3(g), sO$_2$ values measured with traditional PAM deviated from normal physiological condition, while all-fiber PAM maintained a stable sO$_2$ value after three hours. The structural similarity index (SSIM) is also employed to access the similarities between different images. At time 0, the SSIM between the TPAM and FPAM images is 0.7426. After 3 h, the SSIM between TPAM and FPAM results changes to 0.7218, only by 2.8 %; while the SSIM between TPAM image at time 0 and the TPAM image at 3 h is 0.4973, reducing by ~ 50 %. Thus, all-fiber PAM outperforms traditional PAM in terms of long-term stability. Although realignment of the optical fiber coupling or frequent calibration of the laser pulse energy can reduce the sO$_2$ errors in traditional PAM, extra hardware and maintenance costs make the all-fiber approach more advantageous.

All-fiber PAM is equipped with three optical wavelengths. Since the 532 and 545 nm wavelengths are isobestic points for oxy- and

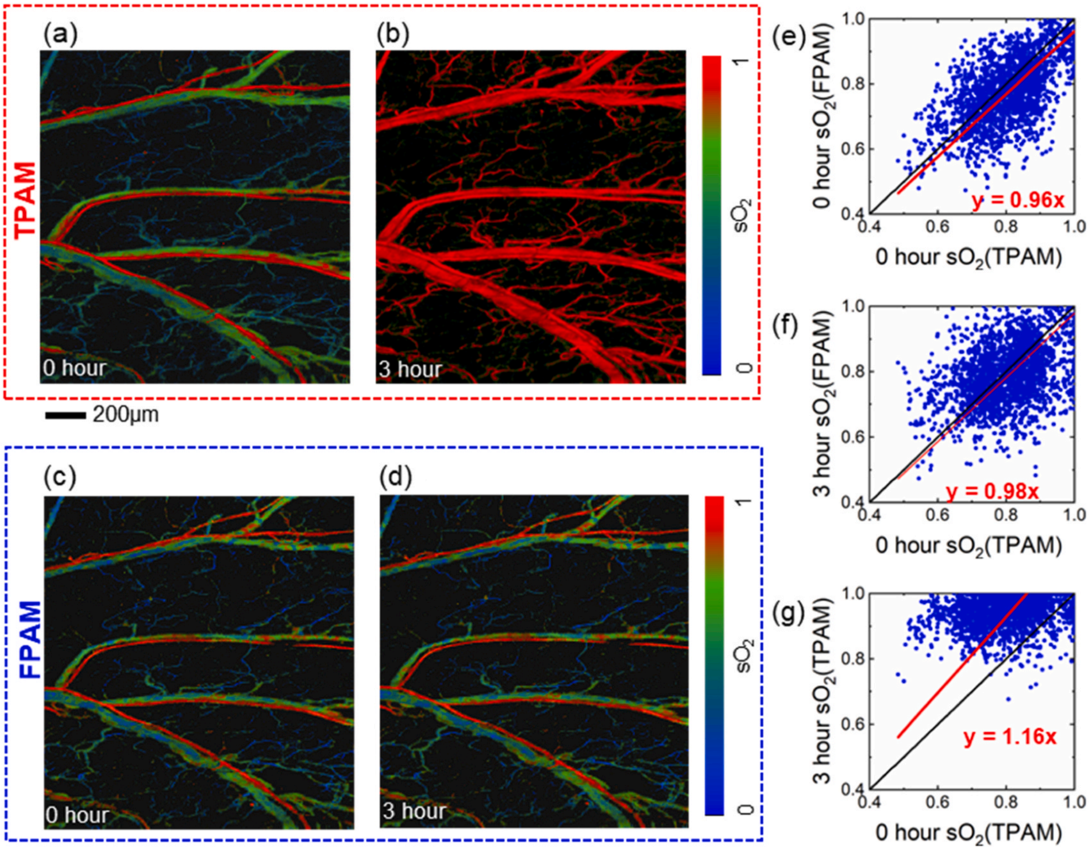

Fig. 3. Long-term stability of functional imaging on the mouse ear. sO$_2$ images from traditional OR-PAM at (a) 0 h and (b) 3 h. sO$_2$ images from all-fiber OR-PAM at (c) 0 h and (d) 3 h. Fig. (e)–(g) are Pixel-to-pixel sO$_2$ comparison between (c),(d),(e) with (a).

deoxyhemoglobin, we can use the first and second photoacoustic signals to calculate the flood speed based on the Grüneisen relaxation effect [16].

We imaged the mouse cerebral cortex. The mice were anesthetized with 1.5 % isoflurane and fixed by a stereotaxic apparatus. We removed the scalp and thinned a small region of the skull with a surgical dental drill to create a cranial window [19]. Then, the window was applied with ultrasound gel and gently topped with a water tank.

As shown in Fig. 4, we can simultaneously image the vascular structure, oxygen saturation, and flow speed. Trunk arteries exhibit higher flow speed than those in small vessels and veins. The gradient change in flow velocity at the branching points of the blood vessels is clearly observed.

3.3. Long-term functional imaging of the brain

Many drugs exhibit prolonged effects on the brain function. All-fiber PAM offers advantages in stability and accuracy, providing an effective tool for monitoring long-term changes in brain activities. Caffeine is one of the most widely used central nervous system stimulants [37]. It acts by binding to adenosine receptors located in various organs, including the central nervous system, heart and blood vessels. Caffeine can raise intracellular calcium levels, stimulating endothelial nitric oxide synthase (eNOS) in endothelial cells and leading to the production of nitric oxide (NO). When NO diffuses into vascular smooth muscle, it induces vasodilation [38]. However, caffeine may also bind directly to receptors on vascular smooth muscle cells, inducing vasoconstriction through similar mechanisms [39]. Thus, the effects of caffeine on hemodynamics and brain function are complex. Imaging hemodynamics and oxygen saturation in the brain over long term is essential for understanding neurovascular coupling and the regulation of cerebral activities. Here, we applied all-fiber PAM to study the long-term brain functional changes with caffeine intake.

Before the experiment, the mice underwent the same surgical procedure as in the previous section. The animals were imaged for approximately 15 min, followed by an intraperitoneal injection of caffeine (40 mg/kg in saline) at time zero. The region of interest was repeatedly imaged until the mouse woke up in approximately 220 min. As shown in Fig. 5(a), we can clearly observe the cortical vasculature at capillary resolution. To quantify the blood flow and sO_2, we unmixed the PA signals into three wavelengths. Then we used 532 and 545-nm images to calculate the flow speed, and calculated the sO_2 images with 532 and 558-nm wavelengths. Fig. 5(b) and (c) illustrate representative images of blood flow and oxygen saturation.

During approximately four hours of monitoring, we recorded changes in the diameter, flow speed, sO_2, and hemoglobin concentration of the major vessels depicted in the figure. The veins and arteries are segmented based on their sO_2 values. The error bars in Fig. 5(e)–(g) represent standard deviations calculated from the baseline images.

Fig. 5(d) selects several representative locations of blood vessels to show the anatomical and functional changes. As Fig. 5(e) shows, the average venous diameter initially increases by up to 6.4 % in the first 100 min. In contrast, the average arterial diameter continuously decreases by 8.0 % in the first 150 min, consistent with previously reported experimental results [40]. Fig. 5(f) shows the change in flow speed, which indicates that, under the influence of caffeine, flow speed in arteries and veins increased by up to 3.7 % and 6.4 % in 100 min. Fig. 5(g) reveals that, within the first 50 min, the average arterial sO_2 decreased from 97.1 % to 92.2 %, while the average venous sO_2 dropped from 77 % to 74.6 %. After that, the arterial and venous sO_2 values slowly returned to 96.6 % and 75.6 % in over the following hours. The trend in sO_2 corroborates findings in other studies, suggesting that the neural excitement induced by caffeine leads to increased oxygen consumption, resulting in decreased cortical sO_2 [41].

4. Conclusion

We present an all-fiber SRS laser for functional PAM. This system offers several advantages. First, the stability of the pulse energy is improved. The all-fiber SRS laser system limits the number of space-to-fiber couplings to a single instance, significantly decreasing the probability of energy fluctuate or drift due to mechanical disturbances and temperature fluctuations. Second, the system is simple and easy to maintain. Compared with the traditional SRS laser using multiple optical components, the all-fiber SRS laser reduces the complexity of optical path and lower the maintenance cost. Third, the all-fiber Raman laser is more compact and cost-effective. To avoid using optical filters, we encode multi-wavelength laser pulses in the temporal and spectral domains and then unmix the detected PA signals. We demonstrate that the long-term drift of the laser pulse energy is less than 2 % in 10 h and demonstrate stable in vivo functional imaging over 3 h. All-fiber PAM provides an effective approach to monitor long-term brain activities, such as the hemodynamic and functional responses to caffeine. We observe obvious changes in vessel diameter, blood flow, and oxygen saturation. All-fiber Raman laser significantly improves the stability and lower the cost of functional OR-PAM, thereby expanding its preclinical and clinical applications.

CRediT authorship contribution statement

Chen Jiangbo: Writing – review & editing, Supervision, Funding acquisition. **Tang Xu:** Writing – review & editing. **Qu Zheng:** Software.

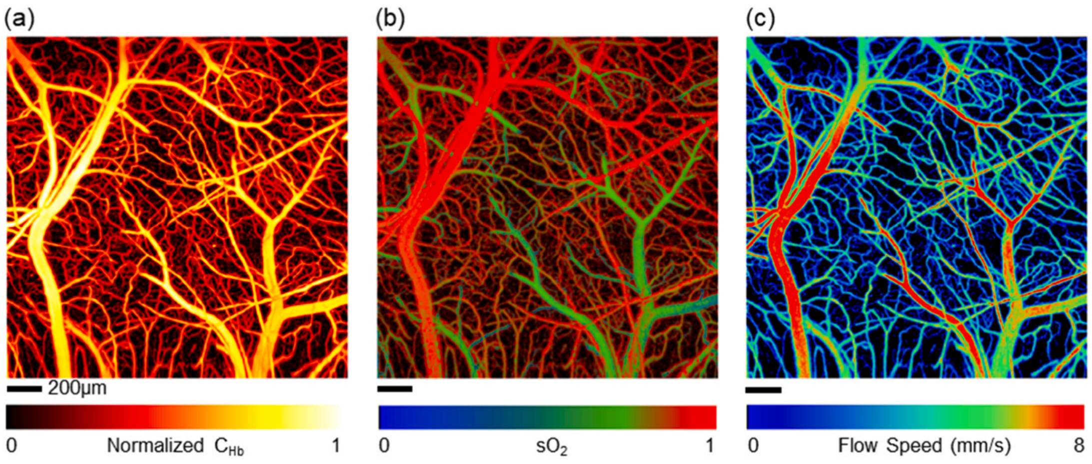

Fig. 4. Functional imaging of the mouse cerebral cortex. Vasculature image. (b) sO_2 image (c) blood flow speed image.

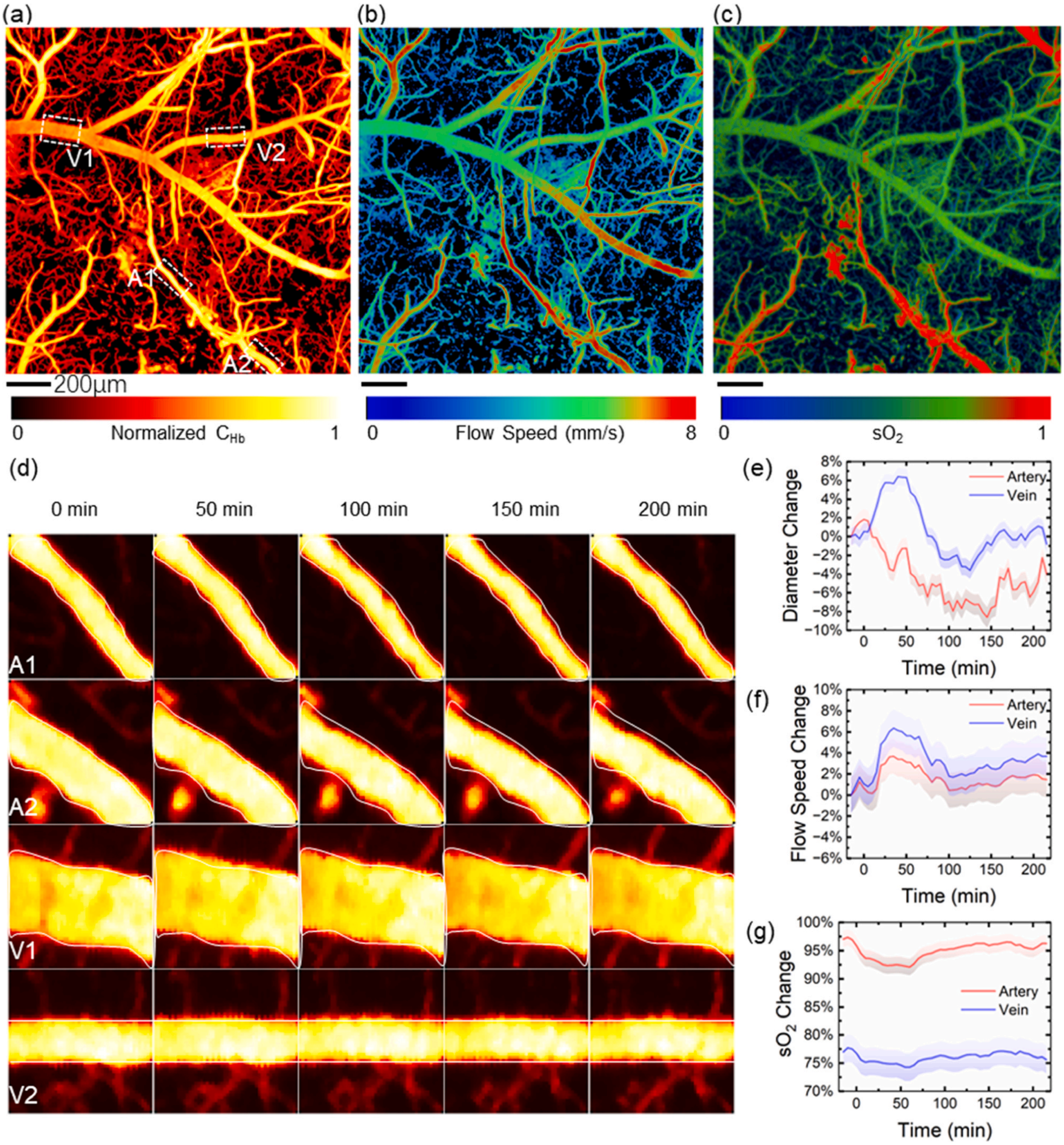

Fig. 5. Mouse cerebral cortex images and monitor results in caffeine administration. (a) Vascular image (b) Flow speed image (c) sO_2 image. (d) The variations of blood vessel structure during the experiments. White solid line delineates the vessel wall. (e) Diameter changes (f) Flow speed changes. (g) sO_2 changes.

YANG Mingxuan: Writing – original draft, Methodology, Data curation. **Amjadian Mohammadreza:** Investigation. **Wang Lidai:** Writing – review & editing, Supervision, Funding acquisition.

Declaration of Competing Interest

The authors declare that they have no known competing financial interests or personal relationships that could have appeared to influence the work reported in this paper.

Acknowledgment

This work is partially supported by the Research Grants Council of the Hong Kong Special Administrative Region (11104922, 11103320), the National Natural Science Foundation of China (NSFC) (81627805, 61805102, 62405093), Guangzhou 2024 Basic and Applied Basic Research Theme Project (SL2023A04J00875), Guangdong Basic and Applied Basic Research Foundation (2023A1515110065).

Data availability

The data that has been used is confidential.

References

[1] L.V. Wang, Tutorial on photoacoustic microscopy and computed tomography, IEEE J. Sel. Top. Quantum Electron. 14 (1) (2023) 171–179, https://doi.org/10.1109/JSTQE.2007.913398.

[2] J. Yao, L.V. Wang, Sensitivity of photoacoustic microscopy, Photoacoustics 2 (2) (2014) 87–101, https://doi.org/10.1016/j.pacs.2014.04.002.

[3] J. Yao, L.V. Wang, Photoacoustic microscopy, Laser Photonics Rev. 7 (5) (2013) 758–778, https://doi.org/10.1002/lpor.201200060.

[4] J. Yao, L. Wang, J. Yang, et al., High-speed label-free functional photoacoustic microscopy of mouse brain in action, Nat. Methods 12 (5) (2015) 407–410, https://doi.org/10.1038/nmeth.3336.

[5] 5C. Taboada, J. Delia, M. Chen, et al., Glassfrogs conceal blood in their liver to maintain transparency, Science 378 (6626) (2022) 1315–1320, https://doi.org/10.1126/science.abl6620.

[6] X. Zhu, Q. Huang, A. DiSpirito1, et al., Real-time whole-brain imaging of hemodynamics and oxygenation at micro-vessel resolution with ultrafast wide-field photoacoustic microscopy, Light Sci. Appl. 11 (1) (2022) 138, https://doi.org/10.1038/s41377-022-00836-2.

[7] Y. Zhou, N. Sun, S. Hu, Deep learning-powered bessel-beam multiparametric photoacoustic microscopy, IEEE Trans. Med. Imaging 41 (12) (2022) 3544–3551, https://doi.org/10.1109/TMI.2022.3188739.

[8] A. Stylogiannis, L. Prade, S. Glasl, et al., Frequency wavelength multiplexed optoacoustic tomography, Nat. Commun. 13 (1) (2022) 4448, https://doi.org/10.1038/s41467-022-32175-6.

[9] Z. Wang, Y. Zhou, S. Hu, Sparse coding-enabled low-fluence multi-parametric photoacoustic microscopy, IEEE Trans. Med. Imaging 41 (4) (2021) 805–814, https://doi.org/10.1109/TMI.2021.3124124.

[10] J. Kim, J.Y. Kim, S. Jeon, et al., Super-resolution localization photoacoustic microscopy using intrinsic red blood cells as contrast absorbers, Light Sci. Appl. 8 (1) (2019) 103, https://doi.org/10.1038/s41377-019-0220-4.

[11] Y. Zhou, L. Wang, J. Chen, et al., Single-shot linear dichroism optical-resolution photoacoustic microscopy, Photoacoustics 16 (2019) 100148, https://doi.org/10.1016/j.pacs.2019.100148.

[12] S. Cheng, Y. Zhou, J. Chen, et al., High-resolution photoacoustic microscopy with deep penetration through learning, Photoacoustics 25 (2022) 100314, https://doi.org/10.1016/j.pacs.2021.100314.

[13] T. Jin, W. Qi, X. Liang, et al., Photoacoustic imaging of brain functions: wide filed-of-view functional imaging with high spatiotemporal resolution, Laser Photonics Rev. 16 (2) (2022) 2100304, https://doi.org/10.1002/lpor.202100304.

[14] W. Zhou, J. He, Y. Li, et al., Multi-focus image fusion with enhancement filtering for robust vascular quantification using photoacoustic microscopy, Opt. Lett. 47 (15) (2022) 3732–3735, https://doi.org/10.1364/ol.459629.

[15] H. Ma, Z. Wang, C. Zuo, et al., Three dimensional confocal photoacoustic dermoscopy with an autofocusing sono-opto probe, J. Biophoton. 15 (5) (2022) e202100323, https://doi.org/10.1002/jbio.202100323.

[16] C. Liu, Y. Liang, L. Wang, Single-shot photoacoustic microscopy of hemoglobin concentration, oxygen saturation, and blood flow in sub-microseconds, Photoacoustics 17 (2020) 100156, https://doi.org/10.1016/j.pacs.2019.100156.

[17] Y. Liang, L. Jin, B.O. Guan, 2 MHz multi-wavelength pulsed laser for functional photoacoustic microscopy, Opt. Lett. 42 (7) (2017) 1452–1455, https://doi.org/10.1364/OL.42.001452.

[18] R. Cao, J. Li, B. Ning, N. Sun, et al., Functional and oxygen-metabolic photoacoustic microscopy of the awake mouse brain, Neuroimage 150 (2017) 77–87, https://doi.org/10.1016/j.neuroimage.2017.01.049.

[19] R. Cao, A. Tran, J. Li, et al., Hemodynamic and oxygen-metabolic responses of the awake mouse brain to hypercapnia revealed by multi-parametric photoacoustic microscopy, J. Cereb. Blood Flow Metab. 41 (10) (2021) 2628–2639, https://doi.org/10.1177/0271678X211010352.

[20] M. Amjadian, S.M. Mostafavi, J. Chen, et al., Super-resolution photoacoustic microscopy via modified phase compounding, IEEE Trans. Med. Imaging 41 (11) (2022) 3411–3420, https://doi.org/10.1109/TMI.2022.3184711.

[21] M. Amjadian, S.M. Mostafavi, J. Chen, et al., Super-resolution photoacoustic microscopy using structured-illumination, IEEE Trans. Med. Imaging 40 (9) (2021) 2197–2207, https://doi.org/10.1109/TMI.2021.3073555.

[22] Y. Zhang, J. Chen, J. Zhang, et al., Super-low-dose functional and molecular photoacoustic microscopy, Adv. Sci. 10 (23) (2023) 2302486, https://doi.org/10.1002/advs.202302486.

[23] X. Zhu, Q. Huang, L. Jiang, et al., Longitudinal intravital imaging of mouse placenta, Sci. Adv. 10 (12) (2024) eadk1278, https://doi.org/10.1126/sciadv.adk1278.

[24] X. Li, K. Yeung, V.T.C. Tsang, et al., Low-cost high-resolution photoacoustic microscopy of blood oxygenation with two laser diodes, Biomed. Opt. Express 13 (7) (2022) 3893–3903, https://doi.org/10.1364/boe.458645.

[25] J. Chen, Y. Zhang, L. He, et al., Wide-field polygon-scanning photoacoustic microscopy of oxygen saturation at 1-MHz A-line rate, Photoacoustics 20 (2020) 100195, https://doi.org/10.1016/j.pacs.2020.100195.

[26] J. Zhu, C. Liu, Y. Liu, et al., Self-fluence-compensated functional photoacoustic microscopy, IEEE Trans. Med. Imaging 40 (12) (2021) 3856–3866, https://doi.org/10.1109/TMI.2021.3099820.

[27] B. Park, M. Han, J. Park, et al., A photoacoustic finder fully integrated with a solid-state dye laser and transparent ultrasound transducer, Photoacoustics 23 (2021) 100290, https://doi.org/10.1016/j.pacs.2021.100290.

[28] L. Li, J. Xia, G. Li, et al., Label-free photoacoustic tomography of whole mouse brain structures ex vivo, Neurophotonics 3 (3) (2016), https://doi.org/10.1117/1.nph.3.3.035001 (035001-035001).

[29] L. Lin, P. Hu, J. Shi, et al., Single-breath-hold photoacoustic computed tomography of the breast, Nat. Commun. 9 (1) (2018) 2352, https://doi.org/10.1038/s41467-018-04576-z.

[30] L. Li, L. Zhu, C. Ma, et al., Single-impulse panoramic photoacoustic computed tomography of small-animal whole-body dynamics at high spatiotemporal resolution, Nat. Biomed. Eng. 1 (5) (2017) 0071, https://doi.org/10.1038/s41551-017-0071.

[31] Z. Wang, F. Yang, H. Ma, et al., Bifocal 532/1064 nm alternately illuminated photoacoustic microscopy for capturing deep vascular morphology in human skin, J. Eur. Acad. Dermatol. Venereol. 36 (1) (2022) 51–59, https://doi.org/10.1111/jdv.17677.

[32] S.W. Cho, S.M. Park, B. Park, et al., High-speed photoacoustic microscopy: a review dedicated on light sources, Photoacoustics 24 (2021) 100291, https://doi.org/10.1016/j.pacs.2021.100291.

[33] Y. He, J. Shi, K.I. Maslov, et al., Wave of single-impulse-stimulated fast initial dip in single vessels of mouse brains imaged by high-speed functional photoacoustic microscopy, J. Biomed. Opt. 25 (6) (2022), https://doi.org/10.1117/1.jbo.25.6.066501 (066501-066501).

[34] J. Chen, Y. ZHANG, X. Li, et al., Confocal visible/NIR photoacoustic microscopy of tumors with structural, functional, and nanoprobe contrasts, Photonics Res. 8 (12) (2020) 1875–1880, https://doi.org/10.1364/prj.409378.

[35] C. Liu, J. Chen, Y. Zhang, et al., Five-wavelength optical-resolution photoacoustic microscopy of blood and lymphatic vessels, Adv. Photonics 3 (1) (2021), https://doi.org/10.1117/1.ap.3.1.016002 (016002-016002).

[36] Z. Qu, C. Liu, J. Zhu, et al., Two-step proximal gradient descent algorithm for photoacoustic signal unmixing, Photoacoustics 27 (2022) 100379, https://doi.org/10.1016/j.pacs.2022.100379.

[37] A. Nehlig, Are we dependent upon coffee and caffeine? A review on human and animal data, Neurosci. Biobehav. Rev. 23 (4) (1999) 563–576, https://doi.org/10.1016/S0149-7634(98)00050-5.

[38] B.E. Sumpio, J.T. Riley, A. Dardik, Cells in focus: endothelial cell, Int. J. Biochem. Cell Biol. 34 (12) (2002) 1508–1512, https://doi.org/10.1016/S1357-2725(02)00075-4.

[39] D. Echeverri, F.R. Montes, M. Cabrera, et al., Caffeine′ s vascular mechanisms of action, Int. J. Vasc. Med. 2010 (1) (2010) 834060, https://doi.org/10.1155/2010/834060.

[40] J.R. Meno, T.S.K. Nguyen, E.M. Jensen, et al., Effect of caffeine on cerebral blood flow response to somatosensory stimulation, J. Cereb. Blood Flow Metab. 25 (6) (2005) 775–784, https://doi.org/10.1038/sj.jcbfm.9600075.

[41] L. Zhou, X. Li, Bin Su, Spatial regulation control of oxygen metabolic consumption in mouse brain, Adv. Sci. 9 (34) (2022) 2204468, https://doi.org/10.1002/advs.202204468.

Mingxuan Yang is a Ph.D. candidate student at the Department of Biomedical Engineering, City University of Hong Kong. He received the Bachelor and Master's degrees from the Harbin institute of Technology. His research focuses on photoacoustic imaging.

Zheng Qu is a Ph.D. candidate student at the Department of Biomedical Engineering, City University of Hong Kong. He received Bachelor's and Master's degrees from Tianjin University. His research focuses on photoacoustic imaging and ultrasound imaging.

Mohammadreza Amjadian is a Postdoctoral Scholar at UC San Diego, specializing in photoacoustic and ultrasound imaging. He holds dual Ph.D. degrees from HKUST and Sharif University of Technology and was a Visiting Researcher at the Biophotonics Lab at City University of Hong Kong, focusing on super-resolution photoacoustic microscopy. His work includes developing wearable biomedical devices and advancing imaging technologies. Dr. Amjadian has published in top journals like IEEE Transactions on Medical Imaging and Optics Express and has received awards such as the HKUST RedBird Academic Excellence Award.

Xu Tang is a Ph.D. candidate student at the Department of Biomedical Engineering, City University of Hong Kong. He received the Bachelor degree from the Beihang University. His research focuses on photoacoustic imaging.

Jiangbo Chen is an Associate professor at the South China University of Technology. He received his Ph.D. degree from the City University of Hong Kong and then worked as a postdoctoral fellow at the Polytechnic University of Hong Kong. He received a Bachelor's degree from Northeast Forestry University and a Master's degree from the Harbin Institute of Technology. His research focuses on biophotonics, biomedical imaging and Non-destructive testing.

Lidai Wang received the Bachelor and Master's degrees from the Tsinghua University, Beijing, and received the Ph.D. degree from the University of Toronto, Canada. After working as a postdoctoral research fellow in the Prof Lihong Wang's group, he joined the City University of Hong Kong in 2015. His research focuses on biophotonics, biomedical imaging, wavefront engineering, instrumentation and their biomedical applications.